Contents lists available at ScienceDirect

Environmental Research

journal homepage: http://ees.elsevier.com

Characterization and assessment of the potential toxicity/pathogenicity of fibrous glaucophane

Dario Di Giuseppe[a,*], Martin Harper[b,c], Mark Bailey[d], Bradley Erskine[e], Giancarlo Della Ventura[f,g], Matteo Ardit[h], Luca Pasquali[i], Gary Tomaino[l], Robyn Ray[m], Harris Mason[n], Melinda D. Dyar[o], Miriam Hanuskova[i], Carlotta Giacobbe[p], Alessandro Zoboli[a], Alessandro F. Gualtieri[a]

[a] Department of Chemical and Geological Sciences, University of Modena and Reggio Emilia, Via Campi 103, Modena, 41125, Italy
[b] Zefon International, Inc., 5350 SW 1st Lane, Ocala, FL, 34474, USA
[c] Department of Environmental Engineering Sciences, University of Florida, Gainesville, FL, 32603, USA
[d] Asbestos TEM Laboratories, 600 Bancroft Way, Suite A, Berkeley, CA, 94710, USA
[e] Kleinfelder, Inc. 401 Marina Place, Benicia, CA, 94510, USA
[f] Department of Sciences, University of Roma Tre, Largo San Leonardo Murialdo 1, Rome, 00146, Italy
[g] INFN Laboratori Nazionali di Frascati, Via E. Fermi 40, I-00044, Frascati, Rome. Italy
[h] Department of Physic and Earth Sciences, University of Ferrara, Via Saragat 1, Ferrara, 44122, Italy
[i] Department of Engineering "Enzo Ferrari", University of Modena and Reggio Emilia, 41125 Modena, Italy
[l] Minerals Technologies Inc., 640 North 13th Street, Easton, PA, 18042, USA
[m] EMSL Analytical, Inc., 200 Route 130 North, Cinnaminson, New Jersey, 08077, USA
[n] Lawrence Livermore National Laboratory, 7000 East Ave. L-231, Livermore, CA, 94550, USA
[o] Department of Astronomy, Mount Holyoke College, 217 Kendade Hall, 50 College St., South Hadley, MA, 01075, USA
[p] European Synchrotron Radiation Facility, 71 Avenue des Martyrs, 38040, Grenoble, France

ARTICLE INFO

Keywords
Mineral fibres
NOA
Glaucophane
California
FPTI

ABSTRACT

In California, the metamorphic blueschist occurrences within the Franciscan Complex are commonly composed of glaucophane, which can be found with a fibrous habit. Fibrous glaucophane's potential toxicity/pathogenicity has never been determined and it has not been considered by the International Agency for Research on Cancer (IARC) as a potential carcinogen to date. Notwithstanding, outcrops hosting fibrous glaucophane are being excavated today in California for building/construction purpose (see for example the Calaveras Dam Replacement Project - CDRP). Dust generated by these excavation activities may expose workforces and the general population to this potential natural hazard. In this work, the potential toxicity/pathogenicity of fibrous glaucophane has been determined using the fibre potential toxicity index (FPTI). This model has been applied to a representative glaucophane-rich sample collected at San Anselmo, Marin County (CA, USA), characterized using a suite of experimental techniques to determine morphometric, crystal-chemical parameters, surface reactivity, biodurability and related parameters. With respect to the asbestos minerals, the FPTI of fibrous glaucophane is remarkably higher than that of chrysotile, and comparable to that of tremolite, thus supporting the application of the precautionary approach when excavating fibrous glaucophane-rich blueschist rocks. Because fibrous glaucophane can be considered a potential health hazard, just like amphibole asbestos, it should be taken into consideration in the standard procedures for the identification and assessment of minerals fibres in soil and air samples.

1. Introduction

Mineral fibres are widespread on Earth where they may occur as flexible poly-filamentous bundles, with individual fibril widths on the micrometre or sub-micrometre scale and splayed ends (Belluso et al., 2017). The mineral fibres that are commercially classified as asbestos are chrysotile, actinolite asbestos, amosite, anthophyllite asbestos, crocidolite, and tremolite asbestos (NIOSH, 1990). Due to their outstanding chemical-physical and technological properties, asbestos minerals have been incorporated in nearly 3000 different composite materials (Gualtieri, 2012). However, long-term epidemiological studies and several animal carcinogenicity tests have provided sufficient scientific evidence that all these six asbestos mineral types, if inhaled, may induce lung diseases like malignant mesothelioma (Skinner et al., 1988). Consequently, the International Agency for Research on Cancer

* Corresponding author.
E-mail address: ddigiuse@unimore.it (D. Di Giuseppe)

https://doi.org/10.1016/j.envres.2019.108723
Received 17 April 2019; Received in revised form 26 August 2019; Accepted 3 September 2019
Available online xxx
0013-9351/

(IARC) included them all in *Group 1* "substance carcinogenic to humans" (Mossman and Churg, 1998; Yarborough, 2007; IARC, 2012) and 55 countries like Italy, France, Germany, Japan, South Africa and Canada have forbidden the importation and use of all asbestos minerals (International Ban Asbestos Secretariat, 2018). Amphibole asbestos is rarely mined today, with a few exceptions, such as in Bolivia where crocidolite (actually magnesio-riebeckite) is still mined and used in asbestos-cement plants (Ilgren et al., 2015) and India, where tremolite asbestos and anthophyllite asbestos are extracted for application in roofing and pipe products (Dave and Beckett, 2005; Ansari et al., 2007). Small quantities of amosite are also reportedly mined in India (Government of India, 2015).

A general concern is growing regarding all mineral species which display a fibrous crystal habit similar to asbestos on the basis that they may be potentially as hazardous as asbestos. The term Elongate Mineral Particles (EMPs) has been coined to include all such particles (National Institute for Occupational Safety and Health (NIOSH), 2011). In addition to the six asbestos minerals, the EMPs have raised global concern as listed below:

(1) The fibrous varieties of the zeolite erionite and the amphibole fluoro-edenite. Up to now, these two species are the only mineral fibres besides asbestos to be classified as carcinogens for humans by the IARC (IARC, 2017, 2012). Epidemiological studies suggest that fibrous erionite and fluoro-edenite are the cause of a high incidence of malignant mesothelioma in some villages in Cappadocia (Turkey) and Sicily (Italy) (Mattioli et al., 2016; Demirer et al., 2015; Carbone et al., 2007; Comba et al., 2003; Paoletti et al., 2000).
(2) Other fibrous amphiboles such as winchite and richterite. Potential risk from these fibrous amphiboles has been proven by several studies (Naik et al., 2017; Baumann et al., 2015). Specifically, they caused an epidemic of lung diseases at Libby, Montana (Baumann and Ambrosi, 2016) although they have not been classified yet in terms of toxicity/carcinogenicity by the IARC.
(3) Other not-listed mineral fibres; e.g. the fibrous zeolite ferrierite. A recent study showed that this zeolite has the same chemical-physical properties that are deemed to prompt adverse effects *in vivo* by fibrous erionite (Gualtieri et al., 2018a). However, no restriction has been considered against fibrous ferrierite because neither toxicity/carcinogenicity nor epidemiological studies have been conducted (Hwang et al., 2013).
(4) Elongated cleavage fragments, i.e. any particle that may have the same chemical formula of the amphibole and serpentine minerals, but which is originated from a crystal that cleaves into fragments rather than being separated longitudinally into fibrils (Gunter et al., 2007). The particles of greatest concern are those which meet the counting criteria of WHO for airborne fibres (length ≥ 5 μm, diameter ≤ 3 μm, length/diameter $\geq 3:1$) (WHO , 1997). However, to date there are no conclusive studies indicating a potential toxicity/pathogenicity or absence of toxicity/pathogenicity for elongate cleavage fragments (Gunter et al., 2007; Weill, 2018).

Potential environmental exposure to respirable mineral dust from natural deposits in which asbestos fibres can be hosted, commonly referred to as naturally occurring asbestos, NOA (Harper, 2008; Lucci et al., 2018) is an issue of great concern in the United States (CARB (California Air Resources Board), 2005; Swayze et al., 2009; DTSC , 2004). In California, NOA occurs in 90% of the counties and many suburban communities are expanding into areas underlain by these deposits (Pan et al., 2005).

Glaucophane, from the Greek "glaukos" (bluish-green) and "phainesthai" (to appear), is an alkaline amphibole whose ideal chemical formula is $Na_2[(Mg,Fe^{2+})_3(Al,Fe^{+3})_2]Si_8O_{22}(OH)_2$ (Deer et al., 2013). Glaucophane is widespread and may occur with a fibrous crystal habit in blueschist facies in former subduction zones or in eclogites that have undergone retrograde metamorphism (Himmelberg and Papike, 1969) such as in Brittany, France and Piedmont, Italy. Although its crystal habit and chemistry make this species analogous to hazardous asbestos amphiboles such as winchite, crocidolite and richterite, its potential toxicity/pathogenicity has never been evaluated to date and this mineral fibre is not classified by the IARC.

A recent investigation (Erskine and Bailey, 2018) has shown that glaucophane in the Franciscan Complex (California, USA) is also fibrous at a micrometre to sub-micrometre level. Franciscan Complex rocks are commonly excavated locally for building/construction purpose in northern and central California (e.g. the Calaveras Dam Replacement Project (CDRP) as well as all developmental projects in the City and County of San Francisco), and the dust generated by the excavation activities may potentially expose construction workers and the nearby populations.

In this study, for the first time, a detailed morphological, chemical and structural characterization of a fibrous glaucophane amphibole is presented with the aim to create a solid basis for future toxicological testing and to evaluate whether this fibre can represent a potential health hazard. To this purpose, the model that predicts a fibre potential toxicity/pathogenicity index (FPTI) proposed by Gualtieri (2018) was used to study fibrous glaucophane from the metamorphic rocks outcropping in San Anselmo, Marin County (USA). The model proposed by Gualtieri (2018) was prompted by the need to better understand the mechanisms by which fibrous minerals, such as those which were mined as asbestos, induce adverse effects *in vivo* (Gualtieri et al., 2017) and is based on the physical, chemical, biological and mineralogical factors that determine the toxicity and pathogenicity. The model (Gualtieri, 2018) permits ranking the potential hazard of unclassified mineral fibres such as the species described in this work. Following the protocol of the FPTI index, a representative sample of fibrous glaucophane from the Franciscan Complex, located north of San Francisco (USA) was characterized using a suite of experimental techniques, to determine morphometric and crystal-chemical parameters, biodurability and related parameters, and surface reactivity (surface iron, Zeta potential, fibres aggregation, etc.).

2. Experimental

2.1. Geological overview and sampling methods

Blueschist is a glaucophane-bearing metamorphic rock typically associated with subduction or continental collision and records metamorphism at high pressures and relatively low temperatures (high-P, low-T) (Wakabayashi, 2015). The most notable and extensively studied blueschist facies terrane in the world is the Franciscan Complex, a diverse 1000 km long belt of oceanic crust and overlying marine and terrestrial sediments that were subducted as the Farallon oceanic plate moved beneath the north American continent in the Jurassic Period, approximately 165 Ma (Wakabayashi, 2015; see Fig. 1 for the distribution of the Franciscan Complex). These rocks are exposed from the California-Oregon border to Los Angeles, California. The Franciscan subduction complex developed from the late Mesozoic to early Tertiary age and consists of penetrative sheared tectonic mélanges and large, relatively coherent rock units (Cowan and Page, 1975). The mélanges contain a diverse assemblage of rocks of various sizes and degrees of metamorphism. The various components include greenstone pillow basalt, blueschist-facies metamorphic rocks, radiolarian chert, fragments of ultramafic mantle rocks, terrigenous greywacke, mudstone, and small amounts of conglomerate (Cloos, 1982). In the regionally metamorphosed Franciscan Complex, blueschist-facies form a narrow belt which extends for more than 400 km along the eastern margin of the Coast Ranges of northern California and southwest Oregon (Wak-

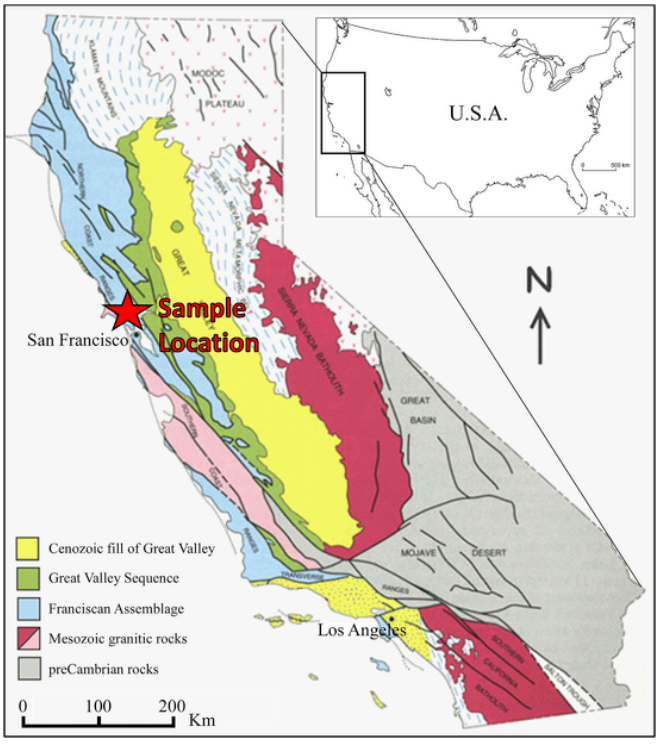

Fig. 1. Sample location and distribution of the Franciscan Complex in California, USA (modified from Irwin, 1990).

abayashi, 2015; Blake et al., 1969). Blueschist rocks commonly occur in the Franciscan Complex at many places along the length of coastal California such as the Tiburon Peninsula, Cazadero area and Marin County (Wakabayashi, 2015; Blake et al., 1969). In the San Francisco bay area region of California, the Franciscan Complex is represented by a variety of tectonic terranes defined by large relatively coherent units separated by thrust or strike-slip faults or broader zones comprised of serpentinitic melange. Some terranes, such as the Alcatraz and Marin Headlands terranes underlying San Francisco and separated by the Hunters Point serpentinite melange, are comprised of relatively low-grade metasediments (ribbon chert, shale, and graywacke sandstone) and metabasalts (greenstone). Within others, such as the Yolla Bolly terrane north and east of San Francisco, rocks have been metamorphosed at higher grades, and include low-temperature high-pressure mineral assemblages including lawsonite, jadeite pyroxene, and glaucophane.

In the present study, blueschist rocks were collected at San Anselmo, Marin County, CA, approximately 24 Km north of San Francisco (see Fig. 1). Glaucophane is the main mineral component and is found in several modes of occurrence within the roughly 30 m diameter high grade block: 1) thin veins within fractured greenstone which can look like blue paint, 2) as an up to approximately 1 m thick rind around the greenstone, and 3) as massive, highly foliated blueschist. Generally, the fibrosity of the material is not visible in hand specimen, or under a hand lens, except within the thin veins in the greenstone where short fibre bundles can be observed. The blueschist sample was prepared at Asbestos TEM Laboratories, Inc. (Berkeley, CA) by crushing, pulverizing and homogenization/mixing (see Erskine and Bailey, 2018, for a full description of the preparation method on a sample from a different location). Approximately 500 g was prepared for this and future research.

2.2. Microscopic characterization, specific surface area and ζ potential

2.2.1. Electron microscopy

To determine the morphometric parameters of the glaucophane fibres, scanning electron microscopy (SEM) analyses were performed using a FEI Nova NanoSEM 450 FEG-SEM with 15 kV accelerating voltage and 3.5 μA beam current and 6 mm working distance. Sample powder obtained by gentle grinding in agate mortar was suspended in distilled water and filtered through a 0.2 mm Nucleopore filter. Half of the filter was placed on an aluminium stub with double-stick carbon tape and sputter-coated with gold (10 nm of thickness), using a Gold Sputter Coater - Emitech K550. Images were acquired using secondary electrons and combined secondary and backscattered electrons (hybrid mode) were used to optimize certain observations. EDX (Energy Dispersive X-ray) data were always collected to confirm the chemical nature of the fibres. A surface of 1 mm^2 of the filter was investigated, collecting 400 random fields at 2000x and down to 10,000x for the chemical and morphometric characterization. The size and morphometric parameters of the single glaucophane particles with an aspect ratio >3 were determined on 244 individuals, counting all the visible particle in the investigated region of interest. Lengths and widths were calculated using ImageJ image analysis software, version 1.52a (NIMH , 2018).

A preliminary transmission electron microscopy (TEM) study was conducted with the aim to investigate the morphology of fibrous glaucophane. A JEOL 1200 EX II (JEOL, Tokyo, Japan) was used at 80 kV, and an XR81-MB Advanced Microscopy Techniques digital camera was utilized to capture the images. The specimen used for the SEM study, obtained by gentle grinding in agate mortar, was suspended in acetone and a drop of suspension was casted on a formvar-coated 200 mesh copper grid and left to dry overnight. Images, EDX data and Selected Area Diffraction images (SAED) were collected on the sample fibre for the identification of the fibre and its morphometric characterization.

2.2.2. Optical microscopy

To determine the optical properties of the glaucophane fibres, observations of the samples were performed both in polarized light and chromatic dispersion technique. Polarized Light Optical Microscopy (PLOM) investigation was performed in transmitted light with an Olympus BX-43 polarizing light microscope equipped with: objective Lenses White LED illumination, circular rotating stage, first order red quarter wavelength compensator plate, Olympus DP73 17 megapixel pixel-shifting digital camera and Olympus Stream Basic 2.1 image collection and processing software. Image magnification was calibrated using stage micrometre 1 mm = 100 × 0.01. Mineral refractive indices were determined using Cargille refractive index oils series A, B & M in conjunction with application of the Becke line method (Faust, 1995).

Phase Contrast Optical Microscopy with chromatic dispersion (PCOM) qualitative analysis was performed using a Leica DM4000 B LED light microscope. Cargille Refractive Index Liquid was used to study the optical properties of the fibres found in the sample (Cavariani et al., 2010).

2.2.3. Determination of the specific surface area (SSA)

SSA of the sample was determined using the BET-method (Brunauer et al., 1938). The SSA analyses were carried out by Gemini V instrument (Micromeritics) with nitrogen as probe gas. About 300 mg of dehydrated sample (at 100 °C for 24 h) was mounted in the sample holder and conditioned at 50 °C prior to measurement. The analysis was carried out using N_2 at the temperature of 77.15 K. Measurements were conducted with an equilibration time of 10 s and the saturation pressure of 777.280 mmHg.

2.3.4. Determination of the ζ potential

The ζ potential of the sample was determined using a Zetasizer Nano Series instrument (Malvern). Analyses were performed using double-distilled water and modified Gamble solution as dispersants. Gamble solution was used to simulate the extracellular environment of the lung and it was prepared following the formulation proposed by Gualtieri et al. (2018b). Sample fibres were added to the dispersants in a weight percentage of 0.1% and subjected to ultrasonic treatment for 15 min ζ potential measurements were conducted at a temperature of 37 °C and different pH. A few drops of HCl 1N were added to the suspension to obtain a pH of 2. The pH was then raised up to 10 using NaOH 0.1 N. The pH was monitored using a Criston Series 2000 pH-meter. ζ potential measurements were collected three times for each sample to check the reproducibility of the results.

2.3. Spectroscopic characterization

2.3.1. Nuclear magnetic resonance (NMR)

^{27}Al NMR spectroscopy was used to determine the coordination of aluminium in the sample (Muller et al., 1981). The ^{27}Al single pulse magic angle spinning nuclear magnetic resonance (SP/MAS NMR) spectra were collected on a Bruker Avance III 600 MHz spectrometer using a double resonance Bruker Very Fast MAS probe configured for 1.3 mm (o.d.) rotors. The sample was spun at a frequency of 35 kHz and data were collected using a 0.5 μs pulse (rf = 47 kHz) and 0.5 or 0.1 s pulse delay (pd) for 1024 to 12,288 scans (ns). The chemical shift was referenced with respect to an external solution of 0.1 M $AlCl_3$ ($\delta_{Al} = 0$ ppm). Due to the presence of Fe in the glaucophane, the ^{27}Al spectra was collected at high spinning rates which reduces the influence of paramagnetic coupling between the ^{27}Al and the Fe in the sample. The fit of the ^{27}Al spectrum modelled using pseudo-Voigt line-shapes and the chemical shifts represents the position of the peak maximum and not the isotropic chemical shift.

2.3.2. Mössbauer spectroscopy

Bulk Fe oxidation state in the sample was determined using the Mössbauer spectroscopy (Gualtieri et al., 2018a). Approximately 70 mg of powder was mixed with sugar in a mortar. Subsequently, the mixture was gently transferred into plastic washers and confined with Kapton tape (Dyar and Burns, 1986). Mössbauer spectra were acquired at temperatures ranging from 4 to 295 K using a source of 100-60 mCi ^{57}Co in Rh on a WEB Research Co. model WT302 spectrometer (Mount Holyoke College). Compton-corrected absorption was calculated for each individual spectrum. Run times were 24 h, and baseline counts were approximately 1 million after the Compton correction. Spectra were collected in 1024 channels and corrected for nonlinearity via interpolation to a linear velocity scale, which is defined by the spectrum of the 25 μm Fe foil used for calibration. Mössbauer spectra were modelled using the Dist_3e program (University of Ghent courtesy of E. DeGrave). The program models spectra using quadrupole splitting or hyperfine field distributions for which the subspectra are constituted by Lorentzian shaped lines. It uses velocity approximations to find the least square minimum between the data and the model using line shape-independent quadrupole splitting of hyperfine field distributions with isomer shift and linewidth as free parameters. Errors on isomer shift are ±0.02–0.03 mm/s for the doublets and sextets in these spectra. Errors on quadrupole splitting and line widths are slightly larger (±0.05 mm/s), and errors on hyperfine fields are ±2–3 kOe (Dyar et al., 2006; Dyar, 1984). Errors on total % of Fe^{3+} are ±1–5% absolute based on repeated fits to the same spectra, with a detection limit for Fe^{3+} of roughly 1%.

2.3.3. Fourier transform infra-red (FTIR) spectroscopy

The FTIR spectrum in the OH-stretching region of the sample was collected with unpolarized light using a Bruker Hyperion 3000 microscope equipped with an MCT detector and a KBr beam splitter. The nominal resolution of set at 4 cm^{-1}, and 128 scans were accumulated for both sample and background.

2.3.4. X-ray photoelectron spectroscopy (XPS)

XPS measurements were conducted with the aim to reveal the Fe^{2+}/Fe^{3+} ratio at the close to surface layers of the glaucophane fibres. XPS spectra were acquired with a CLAM2 VG Microtech electron hemispherical analyser operated at 30 eV of pass energy (0.6 eV of energy resolution) at normal emission and a double anode XR3 VG source, delivering Mg Kα photons (1253.6 eV), at 15 kV, 18 mA.

2.4. Diffraction and chemical data of fibrous glaucophane

2.4.1. X-ray powder diffraction (XRPD) data

High Resolution X-ray synchrotron powder diffraction data were collected at the ID22 beamline of the ESRF (Grenoble, France) using a multi-channel detector. HR-PXRD data were acquired at 31 keV (λ = 0.39994 Å, calibrated with the Si NIST standard SRM 640c at room temperature), with a beam size of 1 mm (horizontal) by 0.9 mm (vertical) defined by water-cooled slits. The beam was monochromated with a cryogenically cooled Si 111 channel-cut crystal. A bank of nine detectors, each preceded by a Si111 analyser crystal, was scanned vertically to measure the diffracted intensity. The capillary was mounted on a rotating support and spun at approximately 2 Hz to improve the powder average. The full profile fitting analyses were performed using XRPD data and Rietveld refinement using the TOPAS package (Coelho, 2018).

2.4.2. Selected area electron diffraction (SAED)

A supplementary SAED TEM study was conducted on the glaucophane fibres. The sample is the same used for the preliminary TEM studies obtained by gentle grinding in agate mortar. The identification and selection of the fibres was supported by imaging and EDX data. Selected Area Electron Diffraction images were acquired on a JEOL 100 CX II Transmission Electron microscope operating at 100 kV using a single tilt sample holder and the smallest aperture to exclude all particulate but the fibre target. SAED were taken with an Olympus side mounted camera. Measurements were made in the Olympus iTEM software in Pixel angstroms and then converted to angstroms using the most recent camera constant. The measured values were compared to both calculated *d*-spacing from the JCPDS card file 23–069 and the experimental values calculated from the Rietveld refinement (see paragraph *2.4.1*). These were supplemented with calculated values using the standard crystallographic equations for the monoclinic systems.

2.4.3. Electron probe micro analysis (EPMA)

Quantitative chemical composition of the sample was obtained using a JEOL 8200 SuperProbe Electron Probe Microanalyzer equipped with a Wavelength-Dispersive X-Ray (WDS) spectrometer system, W hairpin type filament and 1 μm spot size. Detectable element range is 4Be to 92U and detectable wavelength is 0.087–9.3 nm. Atomic number resolution on BSE (Z): less/equal than 0.1 (CuZ). The following analytical conditions were used: excitation voltage of 15 kV, specimen current of 5 nA, peak-count time of 30 s, background-count time of 10 s. The standards utilized were omphacite for Na, elemental vanadium for V, elemental chromium for Cr, elemental copper for Cu, nickeline for Ni, fayalite for Fe, HgSe for Hg, rhodonite for Mn, orthoclase for K, olivine for Mg, grossular garnet for Al, Si and Ca. The instrument is also

equipped with an Energy Dispersive X-Ray Spectroscopy (EDS) system characterized by a detectable element range: ^{11}Na to ^{92}U, energy resolution: 144 eV and lithium (Li)-doped silicon single-crystal semiconductor detector. A fraction of the sample was gently ground in agate mortar and mounted on epoxy discs (25 mm). The discs were polished to expose a cross-section of the material. Prior to analysis, the discs were coated with a thin film of carbon.

Analyses of the individual fibres were not possible because the fibres were invariably aggregated in bundles, clusters and matrices (see the Supplementary material) and the beam spot size was greater than the average fibres' size. The position of each spot analysis was selected using semi-quantitative EDS analysis. The following major elements were determined: K, Na, Ca, Mn, Mg, Fe, Al and Si. The calculation of the crystal-chemical formula was normalized on the basis of 23 O.

2.4.4. ICP-MS

Inductively coupled plasma mass spectrometry (ICP-MS) was used to determine the trace elements (Be, V, Cr, Mn, Co, Ni, Cu, Zn, As and Pb) composition of the sample. The analysis was conducted following the procedure proposed by Bloise et al. (2016). Approximately 50 mg of three different aliquots of sample powder were totally digested with Suprapur® grade of HF and HNO_3 on a hot plate at 200 °C for 8 h. Final solutions were analysed by a quadrupole Thermo X Series-2 ICP-MS spectrometer using kinetic energy discrimination (KED) approach. Calibration curves were made using Merck (Darmstadt, Germany) ICP multi-element standard solution VI (Li, Be, V, Cr, Mn, Co, Ni, Cu, Zn, As, Rb, Sr, Ba, Pb, U, V, Zn). An internal standard (Y) was added to the solutions.

2.4.5. Biodurability

Biodurability of mineral fibres is their ability to resist to chemical/biochemical alteration (Tóth et al., 2016). This property was evaluated by *in vitro* acellular dissolutions tests (Gualtieri et al., 2018b) in batch reactors at 37 °C. In particular, leaching was conducted in Gamble solution (pH = 4) using 25 mg of powder and 250 ml of solution (Gualtieri et al., 2018b). The experiment included six replicates. The degree of dissolution is determined by measuring the change of the sample mass after different times: 48 h, 1 week, 2 weeks, 1-2-3 months. The mass of the sample dissolved with time, was used to determine the apparent dissolution rate R (mol·m^{-2}s^{-1}) from the equation:

$$R = \frac{k}{SSA \cdot m}$$

with SSA determined using the BET-method (see paragraph *2.2.3*), m = initial mass of the sample (g) and k = apparent dissolution rate constant. In addition, assuming that the whole sample consisted of fibres, the estimated lifetime t of a fibre was determined using the equation (originally applied to chrysotile by Hume and Rimstidt, 1992):

$$t = \frac{3w}{4VR}$$

where w = fibre width (m) and V = molar volume (m^3·mol^{-1}). Detailed description of dissolutions test methods and the procedure used for the dissolution data elaboration are reported in Gualtieri et al. (2018b).

2.5. Determination of FPTI of fibrous glaucophane

To calculate the FPTI of fibrous glaucophane and predict its toxic/pathogenic potential, the following parameters are considered (Gualtieri, 2018; Gualtieri et al., 2017): Morphometric parameters (mean fibre length, mean fibre diameter, crystal curvature (if the lattice is cylindrical or not), crystal habit, density, hydrophobic character, specific surface area; Chemical parameters (iron content, content of ferrous iron, surface iron and its nuclearity, content of metals other than iron); Parameters related to biodurability (dissolution rate, rate of iron dissolution/release, rate of silica dissolution/release, rate of release of metals from the fibre); Parameters related to surface reactivity (ζ potential, aggregation state of the fibres in suspension, cation exchange capacity for fibrous zeolite species). Note that for some parameters used the values represent the results from analysing the entire sample, including any minerals other than glaucophane. However, since glaucophane is the major component of the sample (approximately 87%) the results should be close to those which would have been obtained from analysis of pure glaucophane. For each parameter, a score is assigned depending on its measured value and its susceptibility in inducing adverse effects. Because the parameters of the model can be correlated with each other, a hierarchical scheme taking cross-correlations into account is applied (Gualtieri, 2018). A weighing scheme is associated with each parameter of the model according to its step/hierarchy H where $w_1 = 1/H$ with H = 1, 2 or 3. A weight defined as $w_2 = 1/U$ is also applied to each parameter of the model. It accounts for the uncertainty in the determination of a specific parameter (n, m) and is defined by the penalty parameter U (1 = low to null uncertainty, 2 = some degree of uncertainty, 3 = high uncertainty). Having defined the weighing scheme of the parameters, the $FPTI_i$ is calculated according to the equation (Gualtieri, 2018):

$$FPTI_i = \sum_{i=1}^{n} w_1 \cdot w_2 \cdot T_i$$

with T_i = class value of the parameter i of the model; $w_1 = 1/H$ weight of the parameter according to its hierarchy H; $w_2 = 1/U$ weight of the parameter according to the uncertainty U of its determination. Table 1 reports the parameters of the model used for the calculation of the FPTI of fibrous glaucophane, their classification and relative normalized scores $FPTI_i$.

3. Results

A gallery of acquired FEG-SEM and TEM images is reported in Fig. 2. The analyses of the SEM images show that the blueschist is characterized by aggregates of fibrous crystals (Fig. 2a and b) with diameters between 0.04 and 2 μm (average 0.2 μm; Fig. 2b and c), typically arranged in bundles and clusters (Fig. 2a). The bundles exhibit "split-ends" and both individual fibrils and bundles can exhibit slight curvature (Fig. 2a). Clusters and bundles are generally > 20 μm, while the single fibres have a length between 1 and 16 μm with an average of 4 μm (Fig. 2). All of the 244 observed fibres have length/width ratio > 3:1 (the statistics is reported in Table 2). Fig. 2d is an example of SAED pattern of a glaucophane fibre with a relative EDX spectrum.

The quantitative phase analysis performed using XRPD data and the Rietveld method, shows that the blueschist contains glaucophane 86.7(8) wt%, clinochlore 6.4(5) wt%, unclassified amphibole 5.1(7) wt% and minor quartz 1.7(8) wt% (Fig. 3). The agreement indices of the Rietveld quantitative phase analysis are: $R_{exp} = 0.56$, $R_{wp} = 7.86$, $R_p = 5.21$, GOF = 14.04. The graphical output of the Rietveld refinement is shown in the Supplementary material. The refined unit cell parameters of the glaucophane phase in the sample are $a = 9.597(7)$ Å, $b = 17.830(14)$ Å, $c = 5.27(1)$ Å, $\beta = 103.6(6)°$ and V = 876.5(8), matching the values from the literature: $a = 9.541$ Å, $b = 17.740$ Å, $c = 5.295$ Å, $\beta = 103.4°$ and V = 870.9(3) (Papike and Clark, 1968). Given the low amount of the unidentified amphibole species (5.1(7) wt%), a dedicated study is required to assess its very nature.

An example of SAED pattern is reported in Fig. 2d while the indexing of the pattern and the determination of the unit cell parameters, consistent with those of glaucophane, are attached as Supplementary Material.

Table 1
The parameters used and the calculated FPTI for the fibrous glaucophane, Franciscan Complex (CA, USA) and comparison with chrysotile from Balangero (Italy) and asbestos tremolite sample from Val d'Ala (Italy).

Parameters	classes	Normalized score $FPTI_i$	Chrysotile, Balangero (Italy)	Asbestos tremolite, Val D'Ala (Italy)	Fibrous glaucophane, Franciscan Complex (CA, USA)
(1,1) length L	$>5\,\mu m$ and $<10\,\mu m$	0.1	0.4	0.4	0.0
	$>10\,\mu m$ and $<20\,\mu m$	0.2			
	$>20\,\mu m$	0.4			
(1,2) diameter D	$>1\,\mu m$ and $<3\,\mu m$	0.1	0.1	0.1	0.4
	$>0.25\,\mu m$ and $<1\,\mu m$	0.2			
	$>0.25\,\mu m$	0.4			
(1,3) crystal curvature	Flat surface (perfect crystal)	0.05	0.2	0.05	0.05
	Altered surface	0.1			
	Cylindrical surface	0.2			
(1,4) crystal habit	Curled	0.1	0.1	0.4	0.4
	Mixed Curled/acicular	0.2			
	Acicular	0.4			
(1,5) fibre density	$<2.75\,g/cm^3$	0.05	0.05	0.1	0.1
	>2.75 and $<3.5\,g/cm^3$	0.1			
	$>3.5\,g/cm^3$	0.2			
(1,6) hydrophobic character of the surface	Hydrophobic	0.05	0.2	0.2	0.2
	Amphiphilic	0.1			
	hydrophilic	0.2			
(1,7) surface area	$>25\,m^2/g$	0.05	0.05	0.2	0.1
	<25 and $>5\,m^2/g$	0.1			
	$<5\,m^2/g$	0.2			
(1,8) Total iron content	Fe_2O_3+FeO wt% <1	0.05	0.05	0.1	0.2
	$1 < Fe_2O_3+FeO$ wt% < 10	0.1			
	Fe_2O_3+FeO wt% > 10	0.2			
(1,9) ferrous iron	$0 <$ FeO wt% < 0.25	0.05	0.2	0.2	0.2
	$0.25 <$ Fe Owt% < 1	0.1			
	Fe Owt% > 1	0.2			
(1,10) Surface ferrous iron/iron nuclearity	Fe^{2+} nuclearity > 2	0.02	0.03	0.03	0.02
	Fe^{2+} nuclearity $= 2$	0.03			
	Fe^{2+} nuclearity $= 1$	0.07			
(1,11) content of metals other than iron*	$\sum_i \frac{C_i}{L_i} < 1$	0.1	0.4	0.4	0.4
	$1 < \sum_i \frac{C_i}{L_i} < 5$	0.2			
	$\sum_i \frac{C_i}{L_i} > 5$	0.4			
(1,12) dissolution rate log(R)**	$<1y$	0.05	0.05	0.2	0.2
	>1 and $<40y$	0.1			
	$>40y$	0.2			
(1,13) velocity of iron release***	<0.1	0.03	0.07	0.07	0.07
	>0.1 and <1	0.07			
	>1	0.13			
(1,14) velocity of silica dissolution****	<0.5	0.02	0.067	0.03	0.067
	>0.5 and <1	0.03			
	>1	0.07			
(1,15) velocity of release of metals*****	<1	0.03	0.133	0.133	0.133
	>1 and <10	0.07			
	>10	0.13			
(1,16) ζ potential	Negative at pH = 4.5	0.1	0.1	0.2	0.2
	Negative at both pH = 4.5 and 7	0.2			
(1,17) fibres' aggregation	$\varsigma > \|20\|$	0.03	0.033	0.07	0.033
	$\|10\| < \varsigma < \|20\|$	0.07			
	$\|0\| < \varsigma < \|10\|$	0.13			
(1,18) Cation exchange (in zeolites)	cation Exchange	0.07	0	0	0
	no cation exchange	0			
		FPTI (error)	2.23(0.21)	2.88(0.43)	2.77(0.25)

Fig. 4 reports the mineral fibres of the studied sample observed with PLOM. The measured optical parameters of the fibre are reported in Table 3. There are no differences between fibre bundles and clusters as far as the optical properties are concerned.

The ^{27}Al NMR spectrum of blueschist is reported in the Supplementary material. The spectrum shows a peak located at −7.0 ppm, which suggests that Al present in the main minerals is in a six-coordinated (octahedral) environment.

The Fe-Mössbauer spectra of raw material and the extrapolated data are reported in the Supplementary material. The ferrous/ferric ratio of mineral in the blueschist was found to be 65:35.

The results of the EMPA analyses expressed in weight percent with standard deviations are reported in the Supplementary materials. The chemical formula of the fibrous glaucophane, as determined from 45

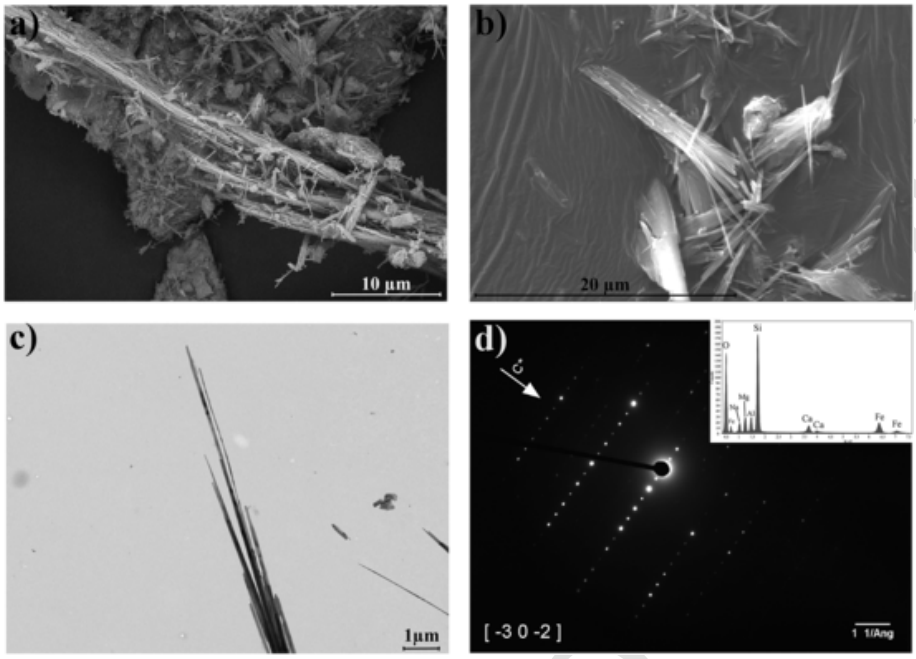

Fig. 2. Representative SEM-FEG (a and b) and TEM (c) images of the glaucophane particles found in the blueschist sample. Glaucophane is characterized by aggregates of fibrils (a, b) with an average diameter of 0.2 µm (b) typically arranged in bundles and cluster (a, b). The bundles exhibit "split-ends" (b, c) and both individual fibrils and bundles can exhibit slight curvature (a, b). Cluster and bundles are generally more than 20 µm long while the single fibres have an average length of 4 µm (b). An example of SAED pattern of a glaucophane fibre with a relative EDX spectrum is reported in (d).

Table 2
Summary statistic of glaucophane fibres geometry. L (length); W (width); Min (minimum); Max (maximum); SD (standard deviation).* Percentile is a value below which a given percentage of values in a data set fall. Example: given a group of observations, the 25th percentile is the value that is greater or equal to 25% of the observations, i.e. the 25% of fibres have L ≤ 2.49 µm, W ≤ 0.16 µm and L/W ≤ 13.0.

	Min	Percentiles*					Max	SD
		5th	25th	50th	75th	95th		
L (µm)	1.10	1.61	2.49	4.00	6.16	9.33	16.2	2.61
W (µm)	0.04	0.10	0.16	0.22	0.30	0.62	1.93	0.21
L/W	3.06	6.12	13.0	18.0	25.8	37.3	72.9	10.5

EMPA spot analyses is:

$$^{A}K^{B}_{0.01}(Na_{1.61}Ca_{0.43})SB\ = 2.04^{C}(Mg_{2.01}Fe^{+2}_{1.31}Fe^{+3}_{0.70}Al_{1.00}Mn_{0.06})SC = 5.08(Si$$

8 analysis spots were also performed on a cluster of ferro-glaucophane. The chemical formula calculated for this amphibole is:

$$^{A}K^{B}_{0.13}(Na_{1.91}Ca_{0.03})SB\ = 1.94^{C}(Mg_{0.89}Fe^{+2}_{1.89}Fe^{+3}_{1.02}Al_{1.15}Mn_{0.03})SC = 4.98(Si$$

Classification of these sodic amphiboles was made according to Hawthorne et al. (2012) using the discriminant atomic ratio Mg/(Mg + Fe^{+2}). In agree with this classification, glaucophane and ferro-glaucophane in the studied blueschist have Mg/(Mg + Fe^{+2}) >0.5 and < 0.5 respectively. Classification plots based on the Mg/(Mg + Fe^{2+}) vs Si content and 100 × Mg/(Mg + Mn + Fe^{2+}) vs

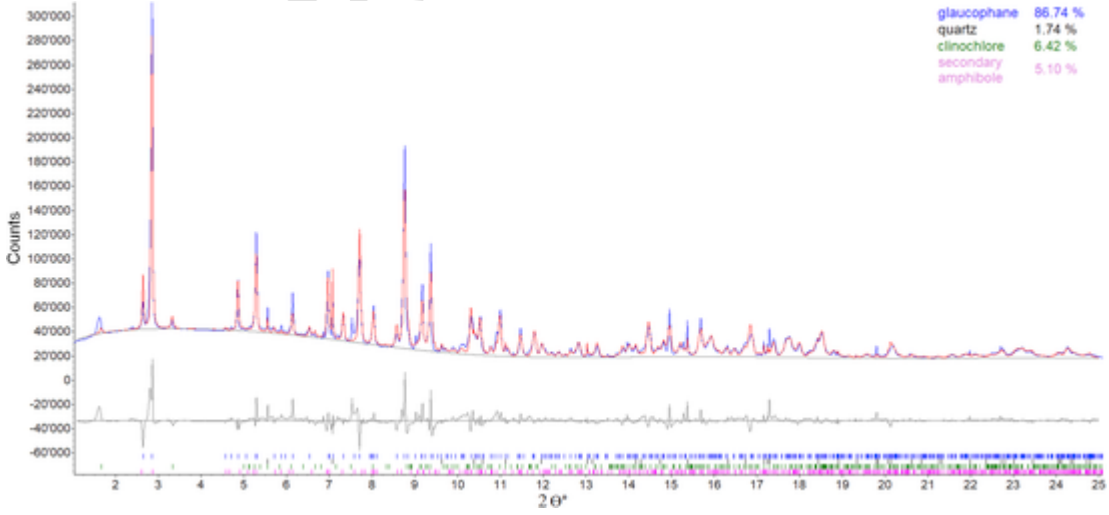

Fig. 3. Rietveld refinement of the X-ray diffraction pattern from the blueschist powder.

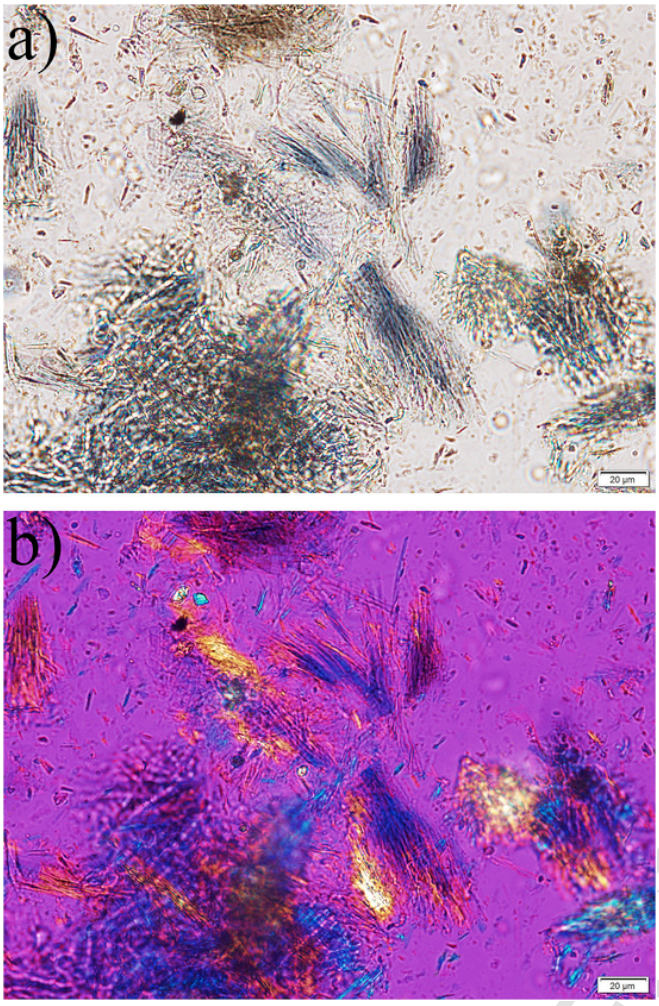

Fig. 4. Mineral fibres observed with PLOM. Glaucophane fibres' bundles (a). Glaucophane aggregates under crossed polars with the compensator plate inserted (b).

Table 3
The optical properties of fibrous glaucophane.

Properties	Values
Colour	Lavender blue
Pleocroism	X = colourless Y = pale blue Z = lavender blue
Sign of elongation	Biaxial (−)
2V	20°
Birefringence	0.009–0.013
Extinction angle	0–14° (undulose extinction)
Colour fibre parallel dispersion staining[a]	Dark blue
Colour fibre perpendicular dispersion staining[a]	Pale Blue
Colour fibre parallel phase contrast[a]	Colourless
Colour fibre perpendicular phase contrast[a]	Colourless
Refractive index n_α	1.636
Refractive index n_β	1.640
Refractive index n_γ	1.644
Delta (n_γ- n_α)	0.008
Dispersion	r < v

[a] Refractive index liquid 1.670.

$100 \times Fe^{3+}/(Fe^{3+} + Al)$ are reported as Supplementary Material (Deer et al., 2013; Leake et al., 1997).

The OH-stretching spectrum of the fibrous glaucophane is given in Fig. 5. The IR spectrum of synthetic end-member glaucophane (Palin et al., 2003; Jenkins and Corona, 2006) shows one single band at 3662 cm^{-1} due to the vibration of O–H groups locally associated with Mg only at the hydroxyl coordinated *M*(1,3) sites. The spectrum of the studied sample, instead, shows the typical four band pattern of amphiboles with Fe^{2+}-Mg at *M*(1,3) (Della Ventura et al., 2005, 2016; Iezzi et al., 2005), and an empty A-site (Della Ventura et al., 2003); in particular, four well resolved peaks are found at 3659, 3647, 3633 and 3616 cm^{-1}, plus an evident shoulder at 3672 cm^{-1}. This pattern is very similar to that of riebeckite (Susta et al., 2018; Della Ventura et al., 2018), an amphibole with a composition very close to glaucophane, the only notable difference being the presence of Fe^{3+} instead of Al at the *M*(2) site. Several particles observed under PLOM also exhibited optical properties (refractive index and sign of elongation) more typical of riebeckite, either in the whole fibre or at one end of a fibre. This is not surprising as glaucophane and riebeckite are end-members of a solid-solution series as magnesium-aluminium (glaucophane) is replaced by ferrous-ferric iron (glaucophane) in the composition. On the basis of the vast literature on amphiboles (Susta et al., 2018; Della Ventura et al., 2018) the observed bands can be assigned to the Mg-MgMg–OH (3659 cm^{-1}), $MgMgFe^{2+}$-OH (3647 cm^{-1}), $MgFe^{2+}Fe^{2+}$-OH (3633 cm^{-1}) and $Fe^{2+}Fe^{2+}Fe^{2+}$-OH (3616 cm^{-1}) configurations. The 3672 cm^{-1} component can be assigned to the MgMgMg–OH configuration close to a B-site locally occupied by Ca (Jenkins et al., 2013) i.e. to a local tremolite-type configuration (Hawthorne et al., 1997, 2000; Della Ventura et al., 2003). At a closer inspection, the higher wavenumber components are broader of the lower wavenumber components; this feature had already been observed in synthetic amphiboles along the tremolite - glaucophane join (Jenkins et al., 2013) and can be assigned to increasing disorder at the B-site, were different cations (Iezzi et al., 2007) are likely to be allocated, i.e. Ca, Mg and Fe^{2+}, in agreement with the EPMA results.

It has been shown (Della Ventura et al., 2016) that the relative intensities of the four components in the IR spectrum of an intermediate Mg–Fe^{2+} amphibole are directly correlated to the relative amounts of the two substituting cations at the *M*(1,3) octahedra. The spectrum shown in Fig. 5 was thus decomposed into single Gaussians, following the procedure discussed by Della Ventura (2017). The result is given in Fig. 6. From the integrated intensities of the fitted components, the amount of Fe^{2+} at *M*(1,3) can be calculated as: $^{M(1,3)}Fe^{2+}$ = IB + 2IC + 3ID, where IB to ID are the intensities of the B to D peaks,

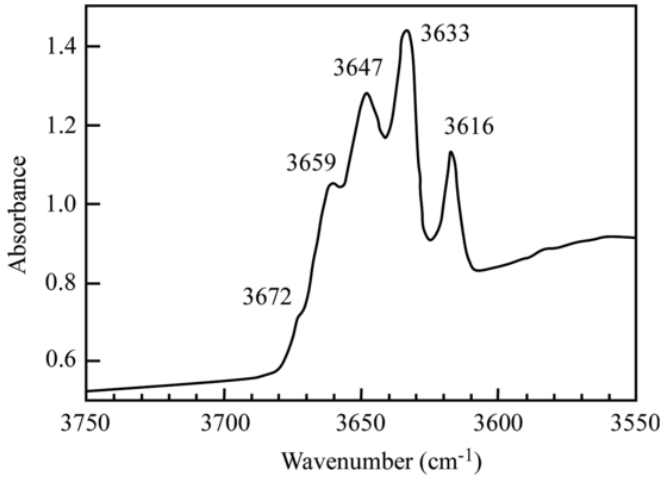

Fig. 5. FTIR OH-stretching spectra of the glaucophane sample.

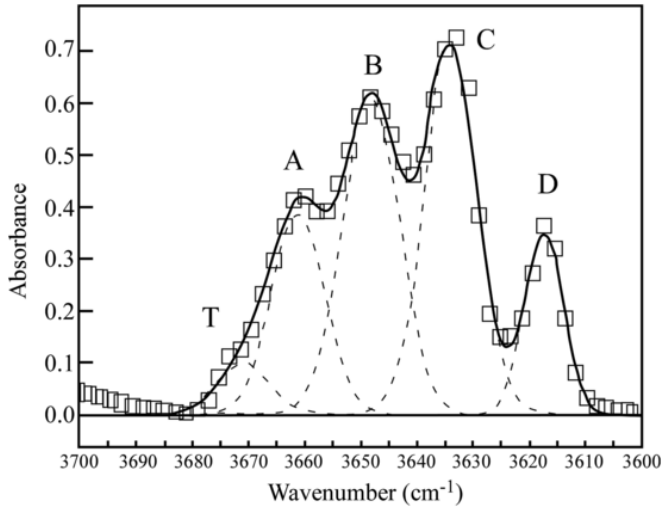

Fig. 6. Fitted FTIR spectrum of the glaucophane sample decomposed using Gaussian components.

respectively (Fig. 6). In the calculations, the intensity of the T ("tremolite") component, due to a local configuration of the type Mg-MgMg–OH–^{B}Ca has been added for simplicity to the intensity of the A component, because the respective OH groups share the same octahedral configuration. The obtained amount of $^{M(1,3)}Fe^{2+}$ is 1.35 a.p.f.u., in excellent agreement with the EPMA results adjusted by the Mössbauer spectroscopy result.

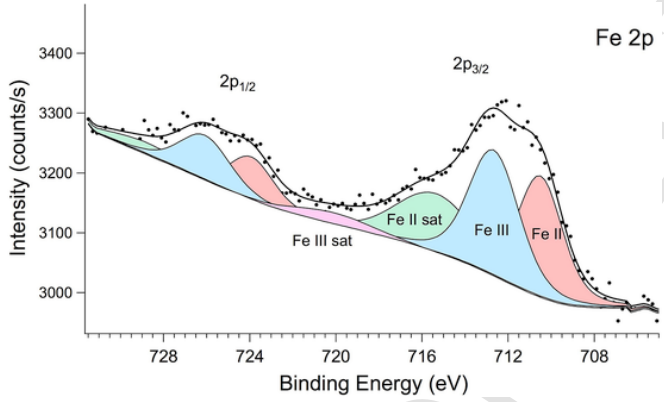

Fig. 7. The Fe2p region of XPS spectra of glaucophane sample.

The XPS spectrum reported in Fig. 7 shows the Fe 2p energy region after subtraction of the Mg X-ray source satellites. The spectrum is decomposed into spin-orbit split Voight doublets, corresponding to $2p_{3/2}$ – $2p_{1/2}$ components, over a Shirley type background. The spectrum presents Fe^{2+} and Fe^{3+} main components, accompanied by related satellites (Grosvenor et al., 2004). The surface Fe^{2+}/Fe^{3+} ratio obtained from XPS peak intensity is 0.88 indicating that the surface of the fibres is oxidized (the Fe^{2+}/Fe^{3+} ratio in bulk glaucophane is 1.87).

Results of the ζ potential analyses as a function of pH are illustrated in Fig. 8. The ζ potential values are all negative and strongly correlated with pH. In the pH range between 2 and 10, the ζ potential of the sample varies from −4 to −37 using double-distilled water as a dispersion media, while from −18 to −28 using Gamble's solution. Nevertheless, the trend of the ζ potential is similar in both dispersion media (see Fig. 8). When the pH of the suspension increases, the ζ potential becomes more negative. Significant differences were only found at highly acidic and alkaline pH conditions. At low pH, the ζ potential is more negative in Gamble's solution with respect to distilled water whereas the opposite is observed at alkaline pH. In both dispersion media, glaucophane shows ζ potential values similar to those found for asbestos amphiboles like crocidolite (Fig. 8b).

SSA of the sample is 7.9 m^2/g. SSA was used to calculate the kinetic parameters of the *in vitro* acellular dissolution (with Gamble solution at pH 4) of glaucophane (Table 1). Dissolution times (t) and dissolution rate (*R*) of glaucophane are comparable with those estimated for the asbestos amphiboles as shown in Table 4.

Table 5 reports the mean values of the content of trace elements measured by ICP-MS. The concentrations are very high if compared with the values found in human lungs (Vanoeteren et al., 1986). Some metals considered as ecological and health risks (As, Co, Cu, Ni, and V) are present in concentrations exceeding recommended limits (Tóth et al., 2016) although this should not represent a concern because the biodurability of the glaucophane amphibole phase prevents their release *in vivo*.

4. Discussion

4.1. Characteristics of fibrous glaucophane

In this study, a thorough characterization is presented on a representative sample of the fibrous glaucophane component of a rock sample obtained from San Anselmo, Marin County, CA (USA). This locality was chosen because of its high concentration of fibrous glaucophane. In fact, the results of the Rietveld quantitative phase and EPMA analyses of the bulk rock confirmed that the blueschist is composed mainly of

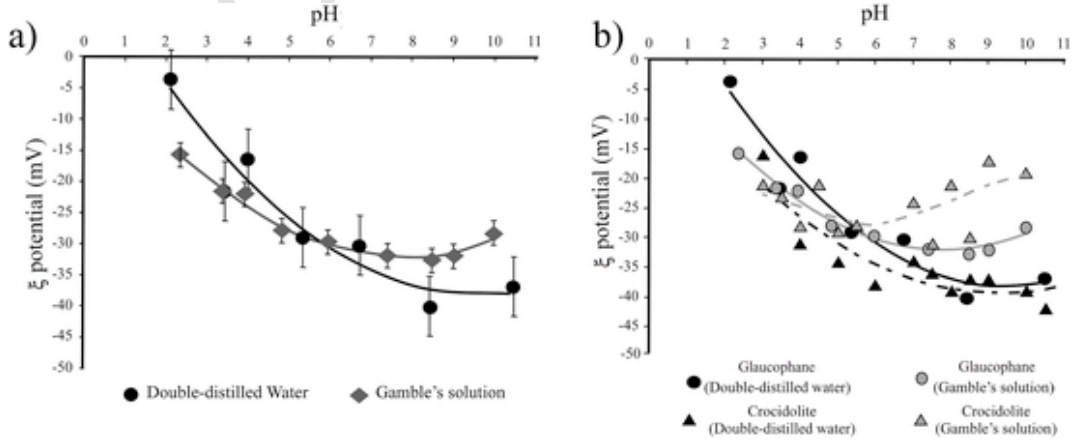

Fig. 8. Plot of the ξ potential versus pH curves. a) fibrous glaucophane in distilled water and Gamble's solution. b) fibrous glaucophane (solid line) and crocidolite (dashed line) in both distilled water and Gamble's solution.

Table 4
Kinetic parameters calculated for the dissolution of mineral fibres.

	SSA (m^2g^{-1})	k (s^{-1})	R ($mol{\cdot}m^{-2}s^{-1}$)	t (days)	t (years)
Glaucophane	7.9	8.2×10^{-13}	4.2×10^{-13}	20,075	55
UICC amosite	9.5	6.1×10^{-13}	2.7×10^{-13}	27,010	74
UICC anthophyllite asbestos	4.4	1.2×10^{-13}	1.0×10^{-13}	83,950	245
UICC crocidolite	16.1	1.3×10^{-13}	3.2×10^{-13}	24,090	66
Val d'Ala tremolite asbestos	9.2	5.4×10^{-14}	4.5×10^{-13}	17,885	49
UICC chrysotile	43	2.5×10^{-10}	2.3×10^{-10}	94	0.3

Table 5
Trace elements concentration (ppm) of the studied blueschist, concentration found in the human lungs (Vanoeteren et al., 1986) and threshold values (Tóth et al., 2016). n.a. (not available).

	Blueschist	Elements in human lungs	Threshold values
V	215	0.50	100
Cr	95.5	0.50	100
Mn	3337	3.00	n.a.
Co	38.2	0.01	20.0
Ni	150	1.00	50.0
Cu	240	5.00	100
Zn	188	30.0	200
As	6.03	0.10	5.00
Pb	8.04	0.50	60.0
Be	7.04	0.03	n.a.

glaucophane with minor ferro-glaucophane and another amphibole of uncertain nature that needs further investigation. In addition, there is a compositional variability across and between some fibres crossing compositional boundaries. This behaviour is common in many amphibole assemblages, for example that found in the vermiculite deposit at Libby, Montana (Lowers et al., 2012). In the optical microscope the mean length of the glaucophane fibres is < 5 μm, but all the fibres display a fibrous habit, with "split-ends", slight curvature and aspect ratio > 3:1, similar to the appearance exhibited by minerals deemed to be asbestos.

Similar to the asbestos amphiboles, glaucophane is biodurable and has negative values of ζ potential at pH 4.5 (Gualtieri et al., 2018b; Pollastri et al., 2014). Negative ξ potential, such as those displayed by of glaucophane may prompt the formation of hydroxyl radicals, affect apoptosis and favour the binding of collagen and redox-activated Fe-rich proteins (Pollastri et al., 2014).

The role of Fe in fibre toxicity is crucial. The total Fe content in the bulk and surface of amphiboles are an important factor for the asbestos-induced patho-biological activity (Gualtieri et al., 2018c). The analysed fibres have a relatively high ferrous (FeO wt% > 1) and total iron (Fe_2O_3 + FeO wt% > 10) content. In addition, XPS analysis showed that both Fe^{+2} and Fe^{+3} are available as structural iron at the surface of the fibres.

4.2. Toxicity/pathogenicity potential of fibrous glaucophane

Table 1 reports the FPTI calculated for fibrous glaucophane and Fig. 9 shows a plot of the FPTI of fibrous glaucophane and other fibrous amphibole species. Following the protocol of the FPTI index, a representative sample of fibrous glaucophane was characterized using a suite of experimental techniques to determine morphometric and chemical parameters, biodurability and related parameters as well as surface reactivity.

The plot reports both the FPTI values calculated assuming the actual morphometric parameters (length L and diameter D) of the fibres (raw) and those calculated assuming ideal values of L > 20 μm and D < 0.25 μm (normalized morphometry) relative to the fibres with the maximum toxicity/pathogenicity potential. The FPTI of fibrous glaucophane is markedly greater than that of chrysotile from the Balangero mine, and comparable to that of amphibole asbestos species like tremolite asbestos from Val d'Ala (Gualtieri, 2018). The results of this calculation clearly indicate that the toxicity/pathogenicity potential of fibrous glaucophane is comparable to that of other amphibole asbestos species, having a value which is very close to that of fibrous fluoro-edenite recently classified as "Carcinogenogenic for Humans" (*Group 1*) by the IARC (IARC, 2012). A closer look at the plot (Fig. 9) reveals that the FPTI of fibrous glaucophane is smaller than that of the other fibrous amphibole species. This is due to the short length L of the individual fibres with the mean value $\bar{L}$ = 4.1 μm smaller than the thresh-

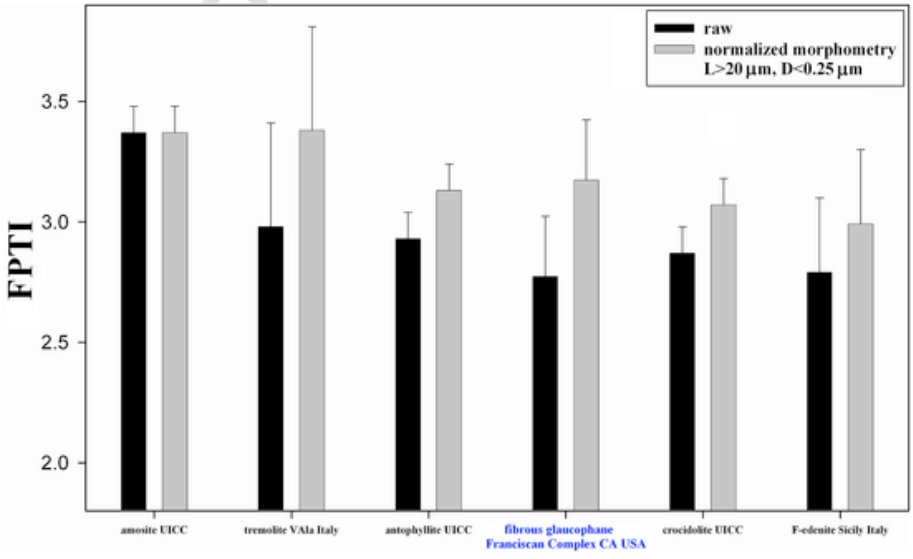

Fig. 9. FPTI calculated for fibrous glaucophane and other fibrous amphibole species.

old limit of 5 μm set for acting successful phagocytosis by alveolar macrophages (Gualtieri et al., 2017). As a matter of fact, our SEM study reveals that the long fibrous glaucophane bundles are basically composed of an intergrowth of short fibre aggregates (clusters) (Fig. 10). If single short fibres released as airborne particulate are respired and reach the deep respiratory system (alveoli), their alveolar phagocytosis and clearance is efficient. A plethora of studies in the literature deals with the issue of the length L of mineral (asbestos) fibres as key parameter in inducing *in vivo* adverse effects. L is one of the key parameters of the fibre toxicity paradigm based on L, D, and biodurability (Pott, 1978) and a key factor in inflammation and pathogenicity of fibres, especially in the development of malignant mesothelioma (MM) (Donaldson et al., 2010). Many researchers in the scientific community believe that short fibres are not hazardous. This model is supported by the 'Stanton hypothesis' (Stanton et al., 1981) indicating that the optimum morphology for inducing intrapleural tumours in rats following injection and implantation is $D \leq 0.25\,\mu m$ and $L > 8\,\mu m$ because longer fibres cannot be eliminated by phagocytic cells leading to frustrated phagocytosis (Churg, 1993). The 'Stanton' model is supported by the evidence that cytotoxicity, inflammatory potential and the development of asbestos-related MMs, lung cancers, and fibrosis are observed with long fibres ($L \geq 5\,\mu m$) that are selectively retained in the lung or pleura (Roggli, 2015). Along the same line, Lippmann (2014) concluded that, for biopersistent airborne fibres, L dictated their ability to cause MM and pulmonary fibrosis or lung cancers with MMs caused by fibres with $L > 5\,\mu m$. Nonetheless, large body of literature have expressed concerns regarding pathogenicity of shorter fibres (Roggli, 2015; Boulanger et al., 2014). Specifically, to date there are no conclusive studies proving the non-fibrogenicity of short ($< 5\,\mu m$) mineral fibres. In this regard, investigations by Nayebzadeh et al. (2006) showed that in the lungs of Québec chrysotile miners the degree of fibrosis is inversely related to the length of the fibres. Subsequent investigations by Adib et al. (2013) underline that the percentage of short fibres in the lungs of miners suffering from fibrosis is slightly larger than the long fibres.

If the assumption that short fibres (i.e. with $L \leq 5\,\mu m$) have limited toxicity/pathogenicity potential, in principle blueschist may have low hazard because of the prevalence of short fibres. Erskine and Bailey (2018) have shown that 6.6% of the fibres found in the air at the Calaveras Dam replacement project are $> 5\,\mu m$ and only 0.6% are $> 10\,\mu m$ long. The weight of L in determining the toxicity/pathogenicity potential of fibrous glaucophane is witnessed by the value assumed by the FPTI if normalized morphometry is considered. In the event that fibrous glaucophane fibres display $L > 20\,\mu m$, their potential toxicity/pathogenicity would be greater than that of asbestos anthophyllite, crocidolite, and fibrous fluoro-edenite.

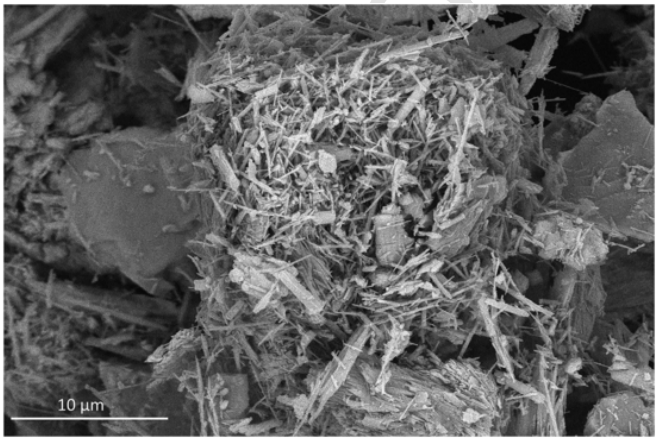

Fig. 10. Representative high-resolution SEM-FEG image of short glaucophane fibre aggregates.

4.3. Implications for the excavation activities in California

The sample from San Anselmo, Marin County (USA) was chosen because of the high concentration of fibrous glaucophane that allowed us to perform its complete characterization and calculation of the FPTI based on the bulk material (the properties of airborne particles liberated by mechanical disturbance of the bulk material may differ from those of the bulk material). The outcome of this study has several implications, as a first step forward to understand the toxicity/pathogenicity and hazardousness of fibrous glaucophane. Although the Marin County locality is 115 Km away from Calaveras Dam site, our study can be useful to support the precautionary approach used during the excavation activities for the CDRP. The characteristics of fibrous glaucophane from Calaveras may be different from those of the Marin County sample. We have also performed a quantitative phase analysis using the Rietveld method (with agreement factors of the refinement $R_{exp} = 4.20\%$; $R_{wp} = 31.66\%$; $R_p = 24.86\%$ and $GOF = 7.54$) on a representative Calaveras sample determined a mineral composition with clinochlore 18.0(8) wt%, amphibole 5.8(1) wt%, fibroferrite 5.8(4) wt%, glaucophane/ferroglaucophane 49.0(1) wt%, lawsonite 18.7(7) wt%, mica 0.7(4) wt%, and quartz 1.9(1) wt%, indicating a comparable mineralogical assemblage. Hence, the outcome of this study justifies a cautious application of the results of the study also to the Calaveras case.

California has the most stringent regulations regarding NOA in excavation of any State in the United States. For sites greater than an acre that have any amount of asbestos, an Asbestos Dust Mitigation Plan must be submitted to the local Air Quality Management Districts, and mandatory dust control measures to prevent asbestos emissions and track-out are required during soil disturbance activities. The California Department of Occupational Safety and Health (DOSH; otherwise known as Cal/OSHA) requires personal protection and exposure control measures when soil with asbestos in any amount at school site is disturbed. However, the mandatory test methods for asbestos, for both soil and air samples, require reporting only of the five "regulated" amphiboles. Laboratories generally exclude glaucophane from test reports because it is not considered "asbestos" and this amphibole species is reported as a non-asbestos mineral or not reported at all.

Soil, perimeter, and personal air monitoring data from the CDRP document the high potential of airborne exposures to the public and site workers from the blueschist amphibole, a mix of amphibole compositions in solid solution with glaucophane being the dominant species (Erskine and Bailey, 2018). During periods of intense blueschist disturbance activities, the concentrations of the blueschist amphibole may routinely exceed perimeter thresholds (based on asbestos risk), and exposures to certain workers may routinely exceed the US federal asbestos permissible exposure limit (PEL). It should be remarked that glaucophane is not a regulated amphibole in California or the US so there is no PEL for exposure to it. PCME structures would be counted by NIOSH 7400 PCM, but further analysis by NIOSH 7402 would have negated the finding (National Institute for Occupational Safety and Health (NIOSH), 1994a; National Institute for Occupational Safety and Health (NIOSH), 1994b). The NIOSH handbook does consider any amphibole in the glaucophane-riebeckite solid solution to be considered hazardous, but the strict regulations do not include glaucophane. Although the blueschist amphiboles are composed predominantly of short fibres (about 7% of the fibres of the CDRP bulk samples are long), it is the number of long fibres in fugitive emissions rather than the percent present in rock and soil that is important.

The potential of adverse exposures to fibrous glaucophane in northern California, as well as other locations where Franciscan rocks are

disturbed, is significant and previously unrecognized. For example, the City and County of San Francisco and majority of the Silicon Valley and surrounding areas to the south are underlain by the Franciscan Complex or Franciscan-derived alluvium. These are areas of intense development, and large construction projects involving commercial buildings and residential subdivisions in close proximity to existing populations are a ubiquitous presence.

5. Conclusions

Glaucophane is a key mineral of blueschist-grade rocks in the Franciscan Complex, and the fibrous habit may be more common than previously recognized (Erskine and Bailey, 2018). The disturbance of blueschist-grade rocks by anthropogenic activities may cause dust emissions that expose workers and population.

Full characterization of the parameters that may be involved in mineral toxicity/pathogenicity cannot be achieved through the application of one or even a few analytical techniques. In this study, fibrous glaucophane was fully characterized using a suite of experimental techniques, and its toxicity/pathogenicity potential was assessed using the FPTI model. The calculated toxicity/pathogenicity potential of fibrous glaucophane is markedly greater than that of chrysotile and comparable to that of asbestos amphibole fibres supporting the application of the precautionary approach when excavation activities regard fibrous glaucophane-rich blueschist rocks. In the future, fibrous glaucophane should be tested *in vitro* to provide experimental confirmation of the outcome of this work. While the findings on the fibrous glaucophane from Marin County may show differences in terms of mineral assemblage and morphology with the sample from Calaveras, our study supports the precautionary approach applied during the excavation activities for the CDRP.

Acknowledgements.

This research was conducted under the Fondi di Ateneo per la Ricerca (FAR 2017) "Fibre potential toxicity Index (FPTI). A quantitative model to evaluate the toxicity and pathogenicity of mineral fibres, including asbestos". The Grant to Department of Science, Roma Tre University (MIUR-Italy Dipartimenti di Eccellenza, ARTICOLO 1, COMMI 314–337 LEGGE 232/2016) is gratefully acknowledged.

Appendix A. Supplementary data

Supplementary data to this article can be found online at https://doi.org/10.1016/j.envres.2019.108723.

$^{*}\sum_{i}\frac{C_i}{L_i}$ = sum of the concentrations of heavy metals (Sb, As, Hg, Cd, Co, Cr, Cu, Pb, Ni, Zn, V, Be) Ci in the fibre (ppm) divided by the limit Li for that metal according to the existing regulatory system (see Table 5) except for Be with limit = 0.5 ppm; **the total dissolution time of the fibre calculated in years (y) following the standardized acellular *in vitro* dissolution model at pH = 4.5 described in reference (Gualtieri et al., 2018b); ***total content of elemental iron in the fibre (wt%) possibly made available as active iron at the surface of the fibre divided by the total dissolution time (y) of the fibre (y); ****total content of Si of the fibre (wt%) divided by the total dissolution time (y) of the fibre; *****total content (ppm) of heavy metals (Sb, As, Hg, Cd, Co, Cr, Cu, Pb, Ni, Zn, V, Be; Mn, Be) divided by the total dissolution time (y) of the fibre.

Uncited reference

Leake et al., 1997.

References

Adib, G., Labrèche, F., De Guire, L., Dion, C., Dufresne, A., 2013. Short, fine and WHO asbestos fibers in the lungs of quebec workers with an asbestos-related disease. Am. J. Ind. Med. 569, 1001–1014.

Ansari, F.A., Ahmad, I., Ashquin, M., Yunus, M., Rahman, Q., 2007. Monitoring and identification of airborne asbestos in unorganized sectors, India. Chemosphere 68, 716–723.

Baumann, F., Ambrosi, J.P., 2016. Environmental non-asbestos related causes of malignant pleural mesothelioma. In: Mineo, T.C. (Ed.), Malignant Pleural Mesothelioma: Present Status and Future Directions, Bentham Science Publishers, Sharjah, pp. 129–144.

Baumann, F., Buck, B.J., Metcalf, R.V., McLaurin, B.T., Merkler, D.J., Carbone, M., 2015. The presence of asbestos in the natural environment is likely related to mesothelioma in young individuals and women from southern Nevada. J. Thorac. Oncol. 10, 731–737.

Belluso, E., Cavallo, A., Halterman, D., 2017. Crystal habit of mineral fibres. In: Gualtieri, A.F. (Ed.), Mineral Fibres: Crystal Chemistry, Chemical-Physical Properties, Biological Interaction and Toxicity, European Mineralogical Union-EMU Notes in Mineralogy, London, pp. 65–109.

Blake, M.C., Irwin, W.P., Coleman, R.G., 1969. Blueschist-facies metamorphism related to regional thrust faulting. Tectonophysics 8, 237–246.

Bloise, A., Barca, D., Gualtieri, A.F., Pollastri, S., Belluso, E., 2016. Trace elements in hazardous mineral fibres. Environ. Pollut. 216, 314–323.

Boulanger, G., Andujar, P., Pairon, J.C., Billon-Galland, M.A., Dion, C., Dumortier, P., Brochard, P., Sobaszek, A., Bartsch, P., Paris, C., Jaurand, M.C., 2014. Quantification of short and long asbestos fibers to assess asbestos exposure: a review of fiber size toxicity. Environ. Health 13, 59.

Brunauer, S., Emmet, P.H., Teller, E., 1938. Adsorption of gases in multimolecular layes. J. Am. Chem. Soc. 60, 309–319.

Carbone, M., Emri, S., Dogan, A.U., Steele, I., Tuncer, M., Pass, H.I., Baris, Y.I., 2007. A mesothelioma epidemic in Cappadocia: scientific developments and unexpected social outcomes. Nat. Rev. Cancer 7, 147–154.

CARB (California Air Resources Board), 2005

CARB (California Air Resources Board)Asbestos airborne toxic control measure for construction, grading, quarrying, and surface mining operationshttps://www.arb.ca.gov/toxics/atcm/asb2atcm.htm200530 October 2018

Cavariani, F., Marconi, A., Sala, O., 2010. Asbestos: sampling, analytical techniques and limit values. Ital. J. Occup. Environ. Hyg. 1, 18–28.

Churg, A., 1993. Asbestos lung burden and disease patterns in man. In: Guthrie, G.D., Mossmann, B.T. (Eds.), Health Effects of Mineral Dust. Reviews in Mineralogy & Geochemistry 28, Mineralogical Society of America and The Geochemical Society, Chantilly, Virginia, USA, pp. 409–426.

Cloos, M., 1982. Flow melanges: numerical modeling and geologic constraints on their origin in the Franciscan subduction complex, California. Geol. Soc. Am. Bull. 93, 330–345.

Coelho, A.A., 2018. TOPAS and TOPAS-Academic: an optimization program integrating computer algebra and crystallographic objects written in C++. J. Appl. Crystallogr. 51, 210–218.

Comba, P., Gianfagna, A., Paoletti, L., 2003. Pleuralmesotheliomacases in Biancavilla are related to a new fluoro-edenite fibrousamphibole. Arch. Environ. Health 58, 229–232.

Cowan, D.S., Page, B.M., 1975. Recycled franciscan material in franciscan mélange west of paso robles, California. Geol. Soc. Am. Bull. 86, 1089–1095.

Dave, S.K., Beckett, W.S., 2005. Occupational asbestos exposure and predictable asbestos-related diseases in India. Am. J. Ind. Med. 48, 137–143.

Deer, W.A., Howie, R.A., Zussman, J., 2013. An Introduction to the Rock-Forming Minerals, third ed. Mineralogical Society of Great Britain and Ireland, London.

Della Ventura, G., 2017. The analysis of asbestos minerals using vibrational spectroscopies (FTIR, Raman): crystal-chemistry, identification and environmental applications. In: Gualtieri, A.F. (Ed.), Mineral Fibres: Crystal Chemistry, Chemical-Physical Properties, Biological Interaction and Toxicity, European Mineralogical Union-EMU Notes in Mineralogy, London, pp. 135–169.

Della Ventura, G., Hawthorne, F.C., Robert, J.L., Iezzi, G., 2003. Synthesis and infrared spectroscopy of amphiboles along the tremolite-pargasite join. Eur. J. Mineral. 15, 341–347.

Della Ventura, G., Milahova, B., Susta, U., Cestelli Guidi, M., Marcelli, A., Schlüter, J., Oberti, R., 2018. The dynamics of Fe oxydation in riebeckite: a model for amphiboles. Am. Mineral. 103, 1103–1111.

Della Ventura, G., Redhammer, G.J., Iezzi, G., Hawthorne, F.C., Papin, A., Robert, J.L., 2005. A Mössbauer and FTIR study of synthetic amphiboles along the magnesioriebeckite-ferri-clinoholmquistite join. Phys. Chem. Miner. 32, 103–113.

Della Ventura, G., Redhammer, G., Robert, J.L., Sergent, J., Iezzi, G., Cavallo, A., 2016. Crystal-chemistry of synthetic amphiboles along the join richterite - ferro-richterite: a combined spectroscopic (FTIR, Mössbauer), XRPD and microchemical study. Can. Mineral. 54, 97–114.

Demirer, E., Ghattas, C.F., Radwan, M.O., Elamin, E.M., 2015. Clinical and prognostic features of erionite-induced malignant mesothelioma. Yonsei Med. J. 56, 311–323.

Donaldson, K., Murphy, F.A., Duffin, R., Poland, C.A., 2010. Asbestos, carbon nanotubes and the pleural mesothelium: a review of the hypothesis regarding the role of long fibre retention in the parietal pleura, inflammation and mesothelioma. Part. Fibre Toxicol. 7, 5.

DTSC (Department of Toxic Substances Control), 2004

DTSC (Department of Toxic Substances Control)Interim guidance naturally occurring asbestos (NOA) at school siteshttps://www.dtsc.ca.gov/Schools/upload/SMBRP_POL_Guidance_Schools_NOA.pdf200430 October 2018

Dyar, M.D., 1984. Precision and interlaboratory reproducibility of measurements of the Mössbauer effect in minerals. Am. Mineral. 69, 1127–1144.

Dyar, M.D., Agresti, D.G., Schaefer, M.W., Grant, C.A., Sklute, E.C., 2006. Mössbauer spectroscopy of Earth and planetary materials. Annu. Rev. Earth Planet Sci. 34, 83–125.

Dyar, M.D., Burns, R.G., 1986. Mössbauer study of ferruginous one-layer trioctahedral micas. Am. Mineral. 71, 955–965.

Erskine, B.G., Bailey, M., 2018. Characterization of asbestiform glaucophane-winchite in the franciscan complex blueschist, northern diablo range, California. Toxicol. Appl. Pharmacol. 361, 3–13.

Faust, R.C., 1995. Refractive index determinations by the central illumination (Becke line) method. P. Phys. Soc. Section B. 68, 1081–1094.

Government of India, 2015

Government of IndiaMinistry of mines, Indian bureau of mines, Indian minerals yearbook, .(Part- III: mineral reviews) 54th edition, asbestos (advance release), January, 2017http://ibm.nic.in/writereaddata/files/01192017155122IMYB2015_Asbestos_19012017_Adv.pdf20153 October 2018

Grosvenor, A.P., Kobe, B.A., Biesinger, M.C., McIntyre, N.S., 2004. Investigation of multiplet splitting of Fe 2p XPS spectra and bonding in iron compounds. Surf. Interface Anal. 36, 1564–1574.

Gualtieri, A.F., 2018. Towards a quantitative model to predict the toxicity/pathogenicity potential of mineral fibers. Toxicol. Appl. Pharmacol. 361, 89–98.

Gualtieri, A.F., 2012. Mineral fibre-based building materials and their health hazards. In: Pacheco-Torgal, F., Jalali, S., Fucic, A. (Eds.), Toxicity of Building Materials, Woodhead, Cambridge, pp. 166–195.

Gualtieri, A.F., Gandolfi, N.B., Passaglia, E., Pollastri, S., Mattioli, M., Giordani, M., Ottaviani, M.F., Cangiotti, M., Bloise, A., Barca, D., Vigliaturo, R., Viani, A., Pasquali, L., Gualtieri, M.L., 2018. Is fibrous ferrierite a potential health hazard? Characterization and comparison with fibrous erionite. Am. Mineral. 103, 1044–1055.

Gualtieri, A.F., Pollastri, S., Bursi Gandolfi, N., Lassinantti Gualtieri, M., 2018. In Vitro Acellular Dissolution of Mineral Fibres: A Comparative Study, Sci Rep-UK, p. 87071.

Gualtieri, A.F., Andreozzi, G.B., Tomatis, M., Turci, F., 2018. Iron from a geochemical viewpoint. Understanding toxicity/pathogenicity mechanisms in iron-bearing minerals with a special attention to mineral fibres. Free Radic. Biol. Med. 133, 21–37.

Gualtieri, A.F., Mossman, B.T., Roggli, V.L., 2017. Towards a general model for predicting the toxicity and pathogenicity of minerals fibres. In: Gualtieri, A.F. (Ed.), Mineral Fibres: Crystal Chemistry, Chemical-Physical Properties, Biological Interaction and Toxicity, European Mineralogical Union-EMU Notes in Mineralogy, London, pp. 501–526.

Gunter, M.E., Belluso, E., Mottana, A., 2007. Amphiboles: environmental and health concerns. Rev. Mineral. Geochem. 67, 453–516.

Harper, M., 2008. Naturally occurring asbestos. 10th anniversary critical review. J. Environ. Monit. 10, 1394–1408.

Hawthorne, F.C., Della Ventura, G., Robert, J.L., Welch, M.D., Raudsepp, M., Jenkins, D.M., 1997. A Rietveld and infrared study of synthetic amphiboles along the potassium-richterite - tremolite join. Am. Mineral. 82, 708–716.

Hawthorne, F.C., Welch, M.D., Della Ventura, G., Shuangxi, L., Robert, J.L., Jenkins, D.M., 2000. Short-range order in synthetic alluminous tremolites: an infrared and triple-quantum MAS NMR study. Am. Mineral. 85, 1716–1724.

Hawthorne, F.C., Oberti, R., Harlow, G.E., Maresch, W.V., Martin, R.F., Schumacher, J.C., Welch, M.D., 2012. Nomenclature of the amphibole supergroup. Am. Mineral. 97, 2031–2048.

Himmelberg, G.R., Papike, J.J., 1969. Coexisting amphiboles from blueschist facies metamorphic rocks. J. Petrol. 10, 102–114.

Hume, L.A., Rimstidt, J.D., 1992. The biodurability of chrysotile asbestos. Am. Mineral. 77, 1125–1128.

Hwang, J., Ramachandran, G., Raynor, P.C., Alexander, B.H., Mandel, J.H., 2013. Comprehensive assessment of exposures to elongate mineral particles in the taconite mining industry. Ann. Occup. Hyg. 57, 966–978.

Some nanomaterials and some fibres, IARC (International Agency for Research on Cancer), 2017. Some nanomaterials and some fibres. IARC Monogr. Eval. Carcinog. Risks Hum. 111, 215–240.

Asbestos (chrysotile, amosite, crocidolite, tremolite, actinolite, and anthophyllite), IARC (International Agency for Research on Cancer), 2012. Asbestos (chrysotile, amosite, crocidolite, tremolite, actinolite, and anthophyllite). IARC Monogr. Eval. Carcinog. Risks Hum. 100C, 219–309.

Iezzi, G., Della Ventura, G., Bellatreccia, F., Lo Mastro, S., Gunther, M.B., 2007. Site occupancy of natural richterite-winchite amphiboles from Libby, Montana, USA: a comparison between FTIR OH-stretching spectroscopy and micro-chemical (EPMA), X-ray diffraction (SREF) and Mössbauer data. Mineral. Mag. 71, 93–104.

Iezzi, G., Della Ventura, G., Hawthorne, F.C., Pedrazzi, G., Robert, J.L., Novembre, D., 2005. The (Mg,Fe^{2+}) substitution in ferri-clinoholmquistite, $Li_2(Mg,Fe^{2+})_3Fe^{3+}{}_2Si_8O_{22}(OH)_2$. Eur. J. Mineral. 17, 733–740.

Ilgren, E.B., Van Orden, D.R., Lee, R.J., Kamiya, Y.M., Hoskins, J.A., 2015. Further studies of Bolivian crocidolite -Part IV: fibre width, fibre drift and their relation to mesothelioma induction: preliminary findings. Epidemiol. Biostat. Public. Health. 12, 1–11.

International Ban Asbestos Secretariat, 2018

International Ban Asbestos SecretariatInternational ban asbestos Secretariathttp://ibasecretariat.org/chron_ban_list.php201831 July 2019

Irwin, W.P., 1990. The San Andreas Fault System, USGS Professional Paper No, California, p. 1515.

Jenkins, D.M., Corona, J.C., 2006. The role of water in the synthesis of glaucophane. Am. Mineral. 91, 1055–1068.

Jenkins, D.M., Della Ventura, G., Oberti, R., Bozhilov, K., 2013. Synthesis and characterization of amphiboles along the tremolite–glaucophane join. Am. Mineral. 98, 580–600.

Leake, B.E., Woolley, A.R., Arps, C.E.S., Birch, W.D., Gilbert, M.C., Grice, J.D., Hawthorne, F.C., Kato, A., Kisch, H.J., Krivovichev, V.G., Linthout, K., Laird, J., Mandarino, J., Maresch, W.V., Nickel, E.H., Schumaker, J.C., Smith, D.C., Stephenson, N.C.N., Ungaretti, L., Whittaker, E.J.W., Youzhi, G., 1997. Nomenclature of amphiboles: report of the subcommittee on amphiboles of the international mineralogical association commission on new minerals and mineral names. Mineral. Mag. 61, 295–321.

Lippmann, M., 2014. Toxicological and epidemiological studies on effects of airborne fibres: coherence and public health implications. Crit. Rev. Toxicol. 44, 643–695.

Lowers, H., Wilson, S.A., Hoefen, T.M., Benzel, W.M., Meeker, G.P., 2012. Preparation and Characterization of “Libby Amphibole” Toxicological Testing Material USGS

Open-File report 2012-1012, Available from: https://pubs.usgs.gov/of/2012/1012/report/OF12-1012.pdf (accessed 29 October 2018).
Lucci, F., Della Ventura, G., Conte, A., Nazzari, M., Scarlato, P., 2018. Naturally occurring asbestos (NOA) in granitoid rocks, a case study from Sardinia (Italy). Minerals 8, 442.
Mattioli, M., Giordani, M., Dogan, M., Cangiotti, M., Avella, G., Giorgi, R., Dogan, A.U., Ottaviani, M.F., 2016. Morpho-chemical characterization and surface properties of carcinogenic zeolite fibres. J. Hazard Mater. 306, 140–148.
Mossman, B.T., Churg, A., 1998. Mechanisms in the pathogenesis of asbestosis and silicosis. Am. J. Respir. Crit. Care Med. 157, 1666–1680.
Muller, D., Gessner, W., Behrens, H.J., Scheler, G., 1981. Determination of the aluminium coordination in aluminium-oxygen compounds by solidstate high-resolution 27Al NMR. Chem. Phys. Lett. 79, 59–62.
Naik, S.L., Lewin, M., Young, R., Dearwent, S.M., Lee, R., 2017. Mortality from asbestos-associated disease in Libby, Montana 1979–2011. J. Expo. Sci. Environ. Epidemiol. 27, 207–213.
Asbestos Fibers and Other Elongate Mineral Particles: State of the Science and Roadmap for Research, National Institute for Occupational Safety and Health (NIOSH), 2011. Asbestos Fibers and Other Elongate Mineral Particles: State of the Science and Roadmap for Research Current Intelligence Bulletin, 62, NIOSH, Cincinnati.
Asbestos and other fibers by phase Contrast microscopy (PCM), National Institute for Occupational Safety and Health (NIOSH), 1994. Asbestos and other fibers by phase Contrast microscopy (PCM). NIOSH Method 7400 (2).
Asbestos by transmission electron microscopy (TEM), National Institute for Occupational Safety and Health (NIOSH), 1994. Asbestos by transmission electron microscopy (TEM). NIOSH Method 7402 (2).
Nayebzadeh, A., Case, B.W., Massé, J., Dufresne, A., 2006. Mineralogical and exposure determinants of pulmonary fibrosis among Quebec chrysotile miners and millers. Int. Arch. Occup. Environ. Health 79, 227–236.
NIMH (National Institute of Mental Health), 2018
NIMH (National Institute of Mental Health)ImageJhttps://imagej.nih.gov/ij/201819 September 2018
Palin, E.J., Guiton, B.S., Craig, M.S., Welch, M.D., Dove, M.T., Redfern, S.A.T., 2003. Computer simulation of Al-Mg ordering in glaucophane and a comparison with infrared spectroscopy. Eur. J. Mineral. 15, 893–901.
Pan, X., Day, H.W., Wang, W., Beckett, L.A., Schenker, M.B., 2005. Residential proximity to naturally occurring asbestos and mesothelioma risk in California. Am. J. Respir. Crit. Care Med. 172, 1019–1025.
Paoletti, L., Batisti, D., Bruno, C., Di Paola, M., Gianfagna, A., Mastrantonio, M., Nesti, M., Comba, P., 2000. Unusually high incidence of malignant pleural mesothelioma in a town of eastern Sicily: an epidemiological and environmental study. Arch. Environ. Health 55, 392–398.
Papike, J.J., Clark, J.R., 1968. The crystal structure and cation distribution of glaucophane. Am. Mineral. 53, 1156–1173.
Pollastri, S., Gualtieri, A.F., Gualtieri, M.L., Hanuskova, M., Cavallo, A., Gaudino, G., 2014. The zeta potential of mineral fibres. J. Hazard Mater. 276, 469–479.
Pott, F., 1978. Some aspects on the dosimetry of the carcinogenic potency of asbestos and other fibrous dusts. Staub Reinhalt. Luft 38, 486–490.
Roggli, V.L., 2015. The so-called short-fiber controversy: literature review and critical analysis. Arch. Pathol. Lab Med. 139, 1052–1057.
Skinner, H.C.W., Ross, M., Frondel, C., 1988. Asbestos and Other Fiberous Materials, Oxford University Press, New York.
Stanton, M.F., Layard, M., Tegeris, M.A., Miller, E., May, M., Morgan, A, E., 1981. Smith, Relation of particle dimension to carcinogenicity in amphibole asbestoses and other fibrous minerals. J. Natl. Cancer Inst. (Bethesda) 67, 965–975.
Susta, U., Della Ventura, G., Hawthorne, F.C., Milahova, B., Oberti, R., 2018. The crystal-chemistry of riebeckite, ideally $Na_2Fe^{2+}3Fe^{3+}{}_2Si_8O_{22}(OH)_2$: a multi-technical study. Mineral. Mag. 82, 837–852.
Swayze, G.A., Kokaly, R.F., Higgins, C.T., Clinkenbeard, J.P., Clark, R.N., Lowers, H.A., Sutley, S.J., 2009. Mapping potentially asbestos-bearing rocks using imaging spectroscopy. Geology 37, 763–766.
Tóth, G., Hermann, T., Da Silva, M.R., Montanarella, L., 2016. Heavy metals in agricultural soils of the European Union with implications for food safety. Environ. Int. 88, 299–309.
Vanoeteren, C., Cornelis, R., Verbeeck, P., 1986. Evaluation of trace elements in human lung tissue III. Correspondence analysis. Sci. Total Environ. 54, 237–245.
Wakabayashi, J., 2015. Anatomy of a subduction complex: architecture of the Franciscan Complex, California, at multiple length and time scales. Int. Geol. Rev. 57, 669–746.
Weill, D., 2018. Proceedings of the Monticello Conference on Elongate Mineral particles (EMP) 361, 1–2.
WHO (World Health Organization), 1997
WHO (World Health Organization)Determination of airborne fibre number concentrationshttp://apps.who.int/iris/bitstream/10665/41904/1/9241544961.pdf199719 September 2018
Yarborough, C.M., 2007. The risk of mesothelioma from exposure to chrysotile asbestos. Curr. Opin. Pulm. Med. 13, 334–338.